On the core-noise analysis coupling of a model gas-turbine combustor and nozzle

By C. X. Shao, K. Maeda AND M. Ihme

1. Motivation and objectives

The understanding, prediction, and mitigation of engine noise have received significant attention due to increasingly stringent requirements for noise-reduction and anticipated growth in air traffic. Engine noise can be categorized as fan noise, jet noise, or core noise. With recent progress toward the reduction of fan noise and jet noise, the relative contribution of core noise has increased in importance. Furthermore, with increasing interest in employing lean premixed combustion technologies and the consideration of compact combustors that operate at higher pressures and power densities (Hultgren 2011), it is anticipated that combustion-generated noise will further increase in importance.

Different mechanisms that contribute to core noise have been identified (Strahle 1978; Candel *et al.* 2009; Dowling & Mahmoudi 2015; Ihme 2017). The first is direct combustion noise, which describes the transmission of pressure fluctuations originating from unsteady heat release in the combustion chamber (Strahle 1978). The second is indirect combustion noise, which is caused by the convection of unsteady vortices and entropy variations by temperature hot spots as they propagate from the combustor to the downstream turbine and nozzle (Marble & Candel 1977). More recently, contributions from mixture inhomogeneities were identified as an additional source of indirect combustion noise that has so far not been considered (Ihme 2017; Magri *et al.* 2016). The relative contributions of these noise-source mechanisms are strongly dependent on operating conditions, engine type, and interaction with other noise-source mechanisms.

Experiments have been conducted to examine combustion noise. With relevance to the analysis of indirect noise, Bake *et al.* (2009) conducted measurements in an entropy wave generator to systematically investigated entropy noise mechanisms. More recently, Rolland *et al.* (2018) performed measurements in a carefully designed entropy wave generator rig to quantify contributions from direct noise, entropy noise, and compositional noise.

Over recent years, significant progress has been made in the theoretical analysis of core noise. Acoustic analogies have been employed for characterizing direct noise and jet-exhaust noise, and different methods have been proposed for modeling indirect noise, which include the compact nozzle theory (Marble & Candel 1977; Cumpsty & Marble 1977), the effective nozzle length method (Stow *et al.* 2002; Goh & Morgans 2011), expansion methods (Duran & Moreau 2013; Duran & Morgans 2015), and non-linear analysis (Huet & Giauque 2013).

With increasing computational resources, multidimensional numerical simulations have been employed to investigate core noise (Ihme 2017). Leyko *et al.* (2009) compared direct and indirect noise mechanisms in a model combustor and found that indirect noise is small for laboratory experiments but increases for more realistic aeronautical engines. By using large-eddy simulation (LES), Papadogiannis *et al.* (2016) assessed entropy noise generated in a high-pressure turbine stage and found that the upstream entropy

noise is reduced due to the choked turbine nozzle guide vane. O'Brien *et al.* (2015) used a hybrid modeling approach to predict the core noise from a system that consists of a combustor, turbine, nozzle and far-field radiation. Livebardon *et al.* (2016) combined LES and actuator disk theory to predict combustion noise in a helicopter engine, confirming the importance of indirect combustion noise.

These experimental and computational investigations have shown that the relative contributions of direct and indirect noise to the overall core-noise radiation strongly depend on engine type and operating conditions, and an integrated engine-flow path representation requires consideration. Therefore, the objective of this study is to develop a hybrid model and investigate the relative importance of core-noise sources in a model gas turbine combustor. The experimental configuration is presented in Section 2. The numerical formulations of the hybrid method are presented in Section 3. Results are analyzed in Section 4, and conclusions are provided in Section 5.

2. Experimental configuration

The geometry that is considered in this study is a model gas-turbine combustor (Weigand *et al.* 2005). Co-swirling dry air at temperature 298 K is supplied to the chamber through a central nozzle and an annular nozzle. Non-swirling methane is fed through 72 channels forming a ring between the air nozzles. The exit planes of the fuel and inner air nozzles are located 4.5 mm below the exit plane of the outer air nozzle, where the latter is defined as reference height $h = 0$. The combustion chamber has a square section of 85×85 mm and height of 114 mm. A conical top plate with a central exhaust tube forms the exhaust gas exit. The operating condition that is considered in this study is close to the lean extinction limit, with thermal power $P_{th} = 7.6$ kW and equivalence ratio for the overall mixture $\Phi_{glob} = 0.55$. This condition corresponds to the overall air mass flow rate of 281 g/min and fuel mass flow rate of 9.0 g/min. The burner is operated at the ambient pressure of 1.0 bar.

3. Numerical method

3.1. *Hybrid method*

A hybrid model is developed to predict the combustion noise in a model combustor-nozzle configuration. The unsteady combustor LES provides mean and perturbation flows as the inflow boundary for the reduced-order nozzle simulation using the Linearized Euler Equation (LEE). The nozzle is represented by a converging-diverging supersonic nozzle, and the flow in the nozzle follows the linear-velocity profile by Duran & Moreau (2013).

3.2. *Combustor simulation*

LES are performed using an unstructured fully compressible finite-volume solver. The characteristic boundary condition is chosen for the air and fuel flow boundaries. The pressure outlet boundary condition is used for the exit plate and the adiabatic wall boundary condition is used for the wall. The turbulent combustion is modeled using the flamelet-progress variable (FPV) model (Pierce & Moin 2004). The Vreman turbulence model is employed in the present simulation. The final form of the LES equations for the FPV approach are written as follows,

$$\begin{aligned}
\widetilde{D}_t\overline{\rho} &= -\overline{\rho}\nabla\cdot\widetilde{\boldsymbol{u}} + \overline{\dot{S}}_\rho,\\
\overline{\rho}\widetilde{D}_t\widetilde{\boldsymbol{u}} &= -\nabla\overline{p} + \nabla\cdot\overline{\boldsymbol{\tau}}_{\nu+t} + \overline{\dot{\boldsymbol{S}}}_m,\\
\overline{\rho}\widetilde{D}_t\widetilde{e}_t &= -\nabla\cdot(\overline{p}\widetilde{\boldsymbol{u}}) + \nabla\cdot(\overline{\boldsymbol{\tau}}_{\nu+t}\cdot\widetilde{\boldsymbol{u}}) - \nabla\cdot\overline{\boldsymbol{q}}_{\nu+t} + \overline{\dot{S}}_e,\\
\overline{\rho}\widetilde{D}_t\widetilde{Z} &= -\nabla\cdot\overline{\boldsymbol{j}}_{Z,\nu+t} + \overline{\dot{S}}_Z,\\
\overline{\rho}\widetilde{D}_t\widetilde{C} &= -\nabla\cdot\overline{\boldsymbol{j}}_{C,\nu+t} + \overline{\rho}\widetilde{\dot{\omega}}_C,
\end{aligned} \tag{3.1}$$

where $\widetilde{D}_t = \partial + \widetilde{\boldsymbol{u}}\cdot\nabla$ is the substantial derivative, ρ is the density, $\boldsymbol{u}$ is the velocity, p is the pressure, e_t is the total energy, Z is the mixture fraction, C is the progress variable, $\boldsymbol{\tau}$ is the viscous stress tensor, $\boldsymbol{q}$ and $\boldsymbol{j}$ are the flux vectors, and $\dot{S}$ is the source term. The computational mesh consists of 3.2 million hex meshes. A constant time step of 50 ns is chosen. After the simulation reaches a steady state, statistics are collected for 30 ms that is corresponding to seven flow through times.

3.3. *Nozzle-flow simulations*

The acoustic transmission through the nozzle is described from the solution of the linearized Euler equations. In the nozzle, the flow variables of the compressible Euler equations with a frozen chemistry can be decomposed into a mean flow and fluctuations around the mean flow. By substituting the decomposed variables and collecting the first-order terms of the fluctuating quantities, the linearized Euler equations can be obtained as

$$\begin{aligned}
\overline{D}_t s' + \boldsymbol{u}'\cdot\nabla\bar{s} &= 0,\\
\overline{D}_t\boldsymbol{u}' + \boldsymbol{u}'\cdot\nabla\boldsymbol{u} + \nabla p'/\bar{\rho} + (p'/\gamma\bar{p} - s'/c_p - \Psi Z')\,\overline{\boldsymbol{u}}\cdot\nabla\overline{\boldsymbol{u}} &= 0,\\
\overline{D}_t p' + \boldsymbol{u}'\cdot\nabla\bar{p} + \gamma\,(\bar{p}\nabla\cdot\boldsymbol{u}' + p'\nabla\cdot\overline{\boldsymbol{u}}) &= 0,\\
\overline{D}_t Z' + \boldsymbol{u}'\cdot\nabla\bar{Z} &= 0,
\end{aligned} \tag{3.2}$$

where s is the entropy, $\boldsymbol{u}$ is the velocity, p is the pressure, Z is the mixture fraction, ρ is the density, c_p is the heat capacity, γ is the ratio of heat capacity, and Ψ is the chemical potential function. The governing equations are non-dimensionalized using the ambient quantities.

Spatial derivatives in the governing equations are discretized using a standard fourth-order central finite-difference scheme. Temporal discretization is performed using the standard fourth-order Runge-Kutta method with a constant time-step size.

In the process of evaluating compositional noise, it is important to accurately calculate the chemical potential function, Ψ, as shown in Eq. (3.2). The chemical potential μ_i of the substance i is the partial derivative of the Gibbs free energy G with respect to the number of substance moles, $\mu_i = (\partial G/\partial n_i)_{T,p,n_{j\neq i}}$. The chemical potential function is then calculated by finite difference from the flamelet table as

$$\Psi = \frac{1}{c_p T}\sum_i \left(\frac{\mu_i}{W_i} - \Delta h_i^\circ\right)\frac{dY_i}{dZ} = \frac{1}{c_p T}\frac{\partial g}{\partial Z}, \tag{3.3}$$

where Δh_i° is the formation enthalpy of the i-th species, W_i is the molecular weight of the i-th species, T is the temperature, Y_i is the mass fraction of the i-th species, and g is the specific Gibbs energy of the mixture. The flamelet table is created at an operating condition $\chi = 1s^{-1}$ (quasi-unstrained condition near equilibrium) that is expected to be close to the condition exiting the gas-turbine combustor. Here, χ is the scalar dissipation

rate that characterizes the degree of straining and is defined as $\chi = 2\alpha|\nabla Z|^2$, where α is the diffusivity of the mixture fraction.

The transmission is predicted in the form of a transfer function that compares the magnitude of an imposed disturbance at the nozzle inlet to the resulting disturbance at the nozzle outlet. In these studies, the transfer function is conveniently expressed in the characteristic form for the downstream and upstream acoustic waves, advected entropy perturbations, and compositional perturbations: $\pi^{\pm} = (p'/\gamma\bar{p} \pm u'/\bar{c})/2$, $\sigma = s'/c_p$, and $\xi = Z'$. The Helmholtz number is also introduced and defined as $He = fL/c$, where f is the perturbation frequency, L is the nozzle length, and c is the speed of sound at the nozzle inlet.

4. Results and discussion

4.1. *Combustor results*

Time-averaged results showing the axial velocity, temperature, mixture fraction, and OH fields are presented in Figure 1. The figure shows that a strong inner recirculation zone is formed near the swirler, and an annular outer recirculation zone is formed near the wall. From the temperature field and OH field, we can see an obvious "V-shape" flame in the combustor. From the mixture fraction field, we can see rapid mixing due to the strong swirl and precessing vortex core. The PIV measurements of temperature, mixture fraction and OH field are also imposed in Figure 1. It is clear that good qualitative agreements are achieved. Quantitatively, we compare the simulation results of axial velocity, temperature and mixture fraction at different height with experimental results, and the comparison results are shown in Figures 2 and 3. It also shows the good agreement between numerical and experimental results. However, quantitatively speaking, there are some discrepancies between the numerical and experimental results, for example, under-prediction of the shear layer intensity. These differences may be attributed to the modeling errors or insufficient resolution in the simulation. At the same time, experimental challenges such as strong reflection due to the annular glass chamber could also lead to this discrepancy. With these situation into consideration, it is believed that the present numerical results are of appropriate quality. The mean quantities obtained through spatio-temporal averaging at the combustor exit are $\overline{p} = 1.01$ bar, $\overline{u} = 12.5$ m/s, and $\overline{Z} = 0.025$. The mean quantities at the combustor exit are used to construct the mean flow in the downstream nozzle.

4.2. *Nozzle flow result*

In order to solve the linearized Euler equation, the mean flow in the nozzle should be provided. The Mach number at the nozzle inlet can be determined by the condition at the combustor exit, that is, $M_a = 0.05$. The Mach number at the nozzle exit is assumed to be 1.5. According to the isentropic flow condition, the mean flow in the nozzle can be determined based on the quantities at the combustor exit and Mach number at nozzle outlet. The mean flow profile is shown in Figure 4. The velocity follows linear profile that is similar with Duran & Moreau (2013). The choke location can be determined based on the correlation between Mach number and space coordinate in the nozzle, and equals 0.72 for the present converging-diverging supersonic nozzle. It should be noted that the realistic nozzle usually have a long diverging region compared to the converging one that is to avoid flow separation at the diverging region. The profile is significantly

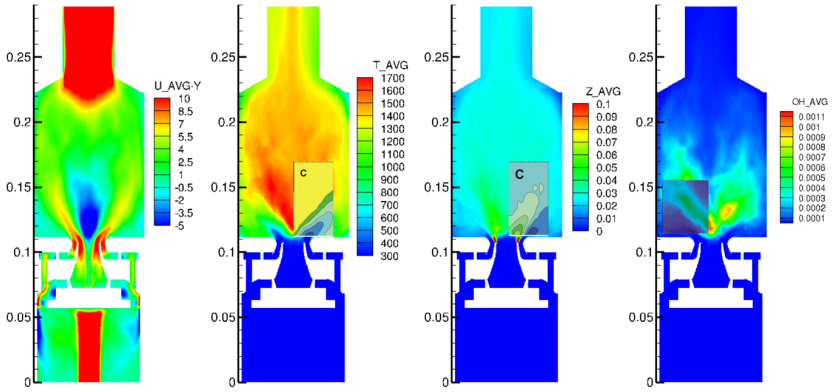

FIGURE 1. Statistical results for axial velocity, temperature, mixture fraction, OH field and their qualitative comparison with experimental results.

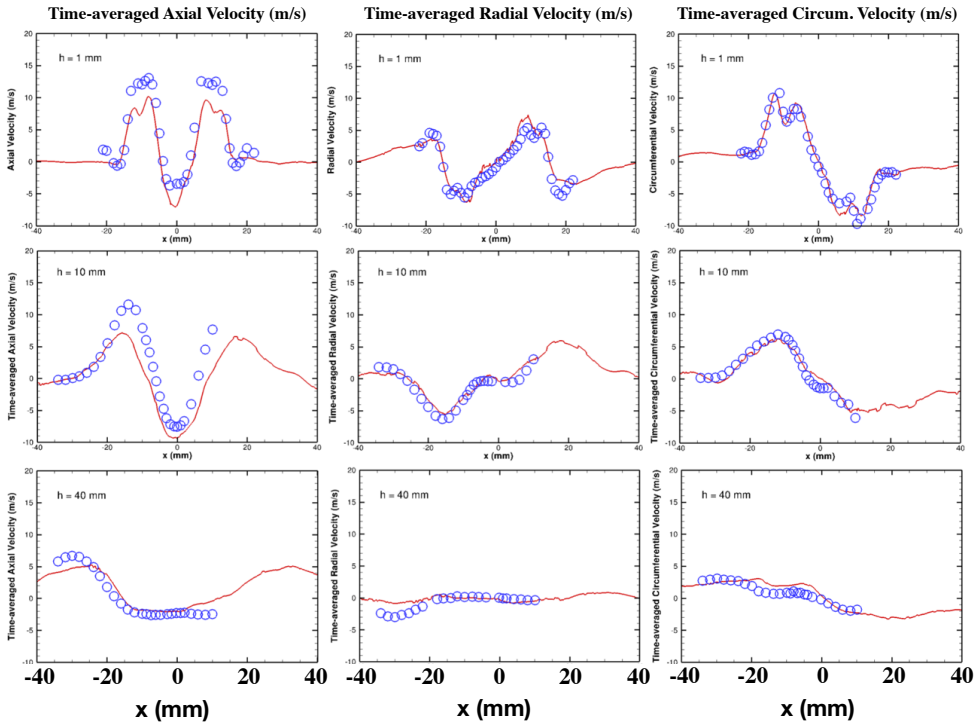

FIGURE 2. Comparison of axial time-averaged velocity between experiment and simulation results at different height, the red lines are the numerical results and the circle dots are the experimental results.

different between the linear nozzle and realistic nozzle. Here we use the linear nozzle just for simplicity. The realistic nozzle geometry will be considered in our future work.

4.3. *Entropy perturbation at nozzle inlet*

We first impose entropy perturbation following the temporally sine profile at the nozzle inlet. The planar entropy perturbation and $He = 2$ are assumed in the present study.

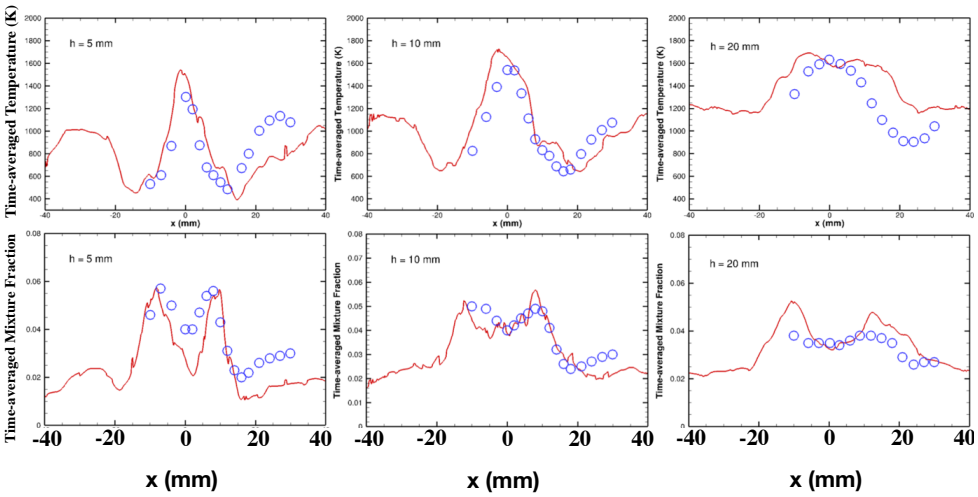

FIGURE 3. Comparison of time-averaged temperature and mixture fraction between experiment and simulation results at different height, the red lines are the numerical results and the circle dots are the experimental results.

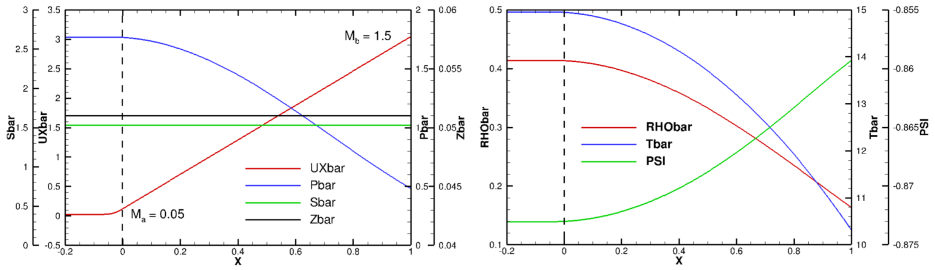

FIGURE 4. The mean flow profile along the nozzle.

The acoustic transmission is described by the change of pressure fluctuation along the nozzle and the sound pressure level can be determined based on the pressure fluctuation at the nozzle exit. The instantaneous pressure fluctuation along the nozzle at the steady state is shown in Figure 5. It can be seen that the amplitude of pressure fluctuation increases along the nozzle, which implies that the entropy perturbation could generate the acoustic wave along the nozzle.

We then show the instantaneous contour of normalized downstream-propagating acoustic wave along the nozzle and the result is displayed in Figure 6. It can be seen that the acoustic wave propagates downstream and the value has no difference along the y-direction due to the planar perturbation imposed at the boundary condition. The magnitude of acoustic wave seems to increase along the nozzle and reach to the maximum at the nozzle exit. The amplitude and phase of the downstream-propagating acoustic wave are then extracted at the nozzle outlet and the results are shown in Figure 7. It shows that the present result is in excellent agreement with the those by Duran & Moreau (2013) and Magri *et al.* (2018). It also shows the compact nozzle theory overestimates the modulus of acoustic wave especially for the large Helmholtz number.

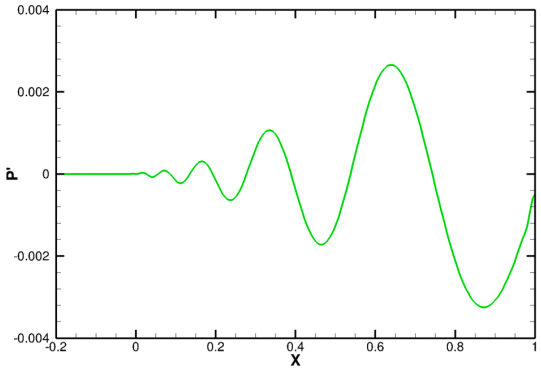

FIGURE 5. The instantaneous pressure fluctuation at the steady state along the nozzle.

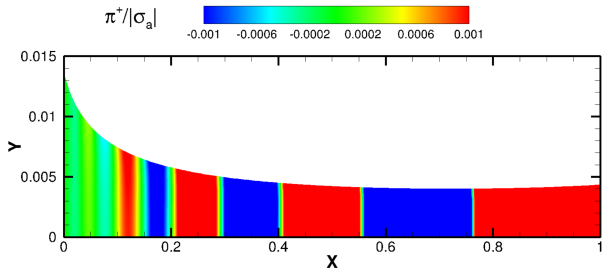

FIGURE 6. The instantaneous contour of normalized downstream-propagating acoustic wave along the nozzle.

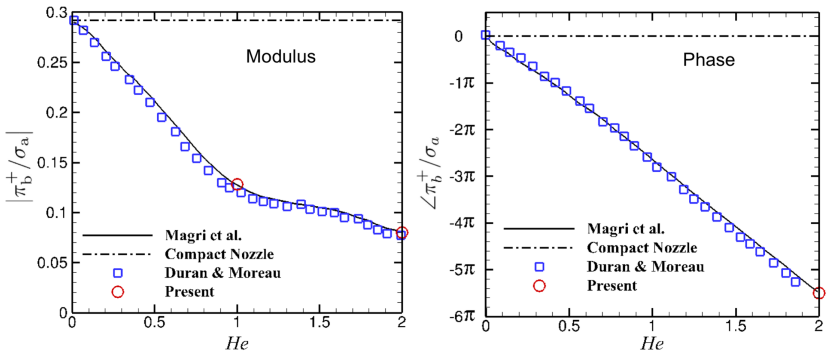

FIGURE 7. The amplitude and phase of the downstream-propagating acoustic wave at the nozzle outlet generated by an incoming entropy wave, and its comparison with theoretical results.

In previous theoretical analyses (Marble & Candel 1977; Cumpsty & Marble 1977; Magri *et al.* 2016; Stow *et al.* 2002; Goh & Morgans 2011; Duran & Moreau 2013; Duran & Morgans 2015) and numerical simulations (Magri *et al.* 2018), perturbation at the nozzle inlet is treated as planar perturbation. However, the spatial distribution at the combustor exit may be different from planar perturbation, which depends on the configuration and combustion conditions. Hence, we investigate the effects of different spatial distributions on the resulting acoustic noise.

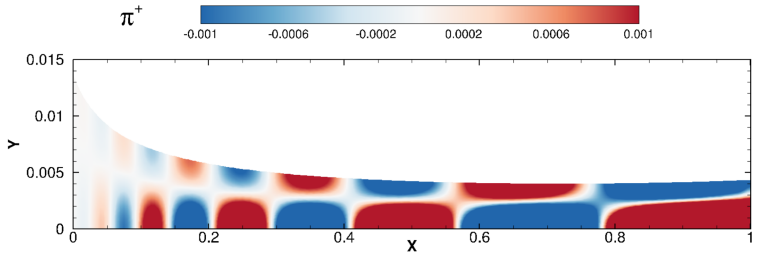

FIGURE 8. The instantaneous contour of normalized downstream-propagating acoustic wave along the nozzle for the Gaussian incoming entropy wave.

We employ the Gaussian distribution of entropy perturbation as the boundary condition for the nozzle inflow. The half-width of Gaussian profile is 0.5. The instantaneous contour of normalized downstream-propagating acoustic wave along the nozzle is shown in Figure 8. It can be seen that the acoustic wave has significant difference along the y-direction. We then calculate the modulus of acoustic wave at the nozzle exit, $\left|\pi_b^+/\sigma_a\right|$, and it equals 0.29 at $He = 2.0$. This is significantly larger than that with 0.18 for planar perturbation. This implies that the spatial mode shape at the combustor exit has significant effects on the acoustic transmission through the nozzle and requires consideration in accurately predicting the resulting combustion noise.

4.4. *Coupling of combustor exit and nozzle flow*

In the LEE simulations described in the previous section, the spatial distribution of the flow variables on the combustor's exit plane was modeled by plane and Gaussian profiles *a priori*. For further accurate coupling, it is desirable to prescribe more realistic boundary conditions. To this aim, one can extract information of the spatial distribution of variables from the LES data, along with its amplitude dependence on the temporal frequency. In this section, we briefly describe a proposed method to prescribe such boundary conditions.

We assume that the flow is homogeneous along the z direction on the exit plane, and dependent only on y and time t. Then we decompose the evolution of flow variable q on the exit plane into the mean and fluctuation as follows

$$q(y,t) = \overline{q}(y) + q'(y,t). \tag{4.1}$$

We further express the fluctuation in terms of temporal frequency as

$$q'(y,t) = \int A_q(y,f) e^{-i(2\pi f t + \phi_q)} df, \tag{4.2}$$

where A_q, f, and ϕ_q are the amplitude, temporal frequency, and phase, respectively.

We adopt two methods to specify the amplitude, A_q. In the first method, we further assume that the variable is uniform along the y direction and prescribe planar distribution of the variable *a priori* as a first-order approximation. We spatially average each flow variable over the combustor's exit plane at each instance of the LES data: $< q' >_y (t) \approx \int q'(y,t)dy/L$, where L is the height of the combustor exit. Then we conduct Fourier transform of $< q' >_y$ to obtain the spatial-averaged amplitude spectrum, $< A_q >_y (f) = FFT[< q' >_y (t)]$. We can conduct LEE simulations with various Mach numbers and various frequencies using this method.

In the second method, we can focus on the component of fluctuations at the characteristic frequency of the combustor noise, $f = f_c$. To this aim, we first apply to the LES

data a band-pass filter to extract the corresponding frequency component of the flow variable on the combustor's exit plane. Then we apply proper orthogonal decomposition (POD) to the filtered data, and use the first spatial POD mode to prescribe the spatial dependence of A_q. This course of analysis has been employed in our recent study to couple simulations of a combustor and a nozzle with different parameters from the present study (Shao *et al.* 2019).

POD is a modal decomposition technique that can extract coherent structures from spatio-temporal dynamical data (Holmes *et al.* 2012). POD of the variable $q'(y,t)$ is given as

$$q'(y,t) = \sum_{i}^{N} \psi_i(y)\phi_i(t), \tag{4.3}$$

where $\psi_i(y)$ and $\phi_i(t)$ are the i-th spatial and temporal POD modes, respectively. The first spatial POD mode, $\psi_1(y)$, contains the most energy and typically represents the coherent spatial variation of q'. Note that, in the present analysis, POD is separately conducted for p', u', s', and z' to extract the first POD mode of each of the variables.

5. Conclusions

In this study, the effect of spatial structure on the acoustic transmission is examined by using a hybrid method to couple the combustor and converging-diverging nozzle. From the present study, the following conclusions can be drawn: (1)The linearized Euler equation is necessary to accurately predict the acoustic transmission due to the radial difference; (2)The spatial mode shape at the combustor exit has significant effects on the acoustic transmission through the nozzle and requires consideration in accurately predicting the resulting combustion noise; (3)The coupling between combustor exit and nozzle flow should be further considered. This is a course of our future work.

Acknowledgments

This investigation was funded by the AeroAcoustics Research Consortium with award number OAI-AARCS-19026. K.M. acknowledges NASA. We thank Dr. Jeonglae Kim for sharing the LEE-solver, and Danyal Mohaddes and Dr. Quentin Douasbin are acknowledged for fruitful discussions on the acoustic analysis.

REFERENCES

Bake, F., Richter, C., Mühlbauer, C., Kings, N., Röhle, I., Thiele, F. & Noll, B. 2009 The entropy wave generator (EWG): A reference case on entropy noise. *J. Sound Vib.* **326**, 574–598.

Candel, S., Durox, D., Ducruix, S., Birbaud, A.-L., Noiray, N. & Schuller, T. 2009 Flame dynamics and combustion noise: progress and challenges. *Int. J. Aeroacoustics* **8**, 1–56.

Cumpsty, N. A. & Marble, F. E. 1977 Core noise from gas turbine exhausts. *J. Sound Vib.* **54**, 297–309.

Dowling, A. P. & Mahmoudi, Y. 2015 Combustion noise. *Proc. Combust. Inst.* **35**, 65–100.

Duran, I. & Moreau, S. 2013 Solution of the quasi-one-dimensional linearized euler

equations using flow invariants and the Magnus expansion. *J. Fluid Mech.* **723**, 190–231.

Duran, I. & Morgans, A. S. 2015 On the reflection and transmission of circumferential waves through nozzles. *J. Fluid Mech.* **773**, 137–153.

Goh, C. S. & Morgans, A. S. 2011 Phase prediction of the response of choked nozzles to entropy and acoustic disturbances. *J. Sound Vib.* **330**, 5184–5198.

Holmes, P., Lumley, J. L., Berkooz, G. & Rowley, C. W. 2012 *Turbulence, Coherent Structures, Dynamical Systems, and Symmetry*. Cambridge: Cambridge University Press.

Huet, M. & Giauque, A. 2013 A nonlinear model for indirect combustion noise through a compact nozzle. *J. Fluid Mech.* **733**, 268–301.

Hultgren, L. S. 2011 Core noise: Implications of emerging N+3 designs and acoustic technology needs. Tech. Rep. E-17796, Acoust. Tech. Working Group, NASA Glenn Res. Cent., Cleveland OH.

Ihme, M. 2017 Combustion and engine-core noise. *Annu. Rev. Fluid Mech.* **49**, 277–310.

Leyko, M., Nicoud, F. & Poinsot, T. 2009 Comparison of direct and indirect combustion noise mechanisms in a model combustor. *AIAA J.* **47**, 2709–2716.

Livebardon, T., Moreau, S., Gicquel, L., Poinsot, T. & Bouty, E. 2016 Combining les of combustion chamber and an actuator disk theory to predict combustion noise in a helicopter engine. *Combust. Flame* **165**, 272–287.

Magri, L., O'Brien, J. & Ihme, M. 2016 Compositional inhomogeneities as a source of indirect combustion noise. *J. Fluid Mech.* **799**, R4.

Magri, L., O'Brien, J. & Ihme, M. 2018 Effects of nozzle Helmholtz number on indirect combustion noise by compositional perturbations. *J. Eng. Gas Turbines Power* **140**, 1–9.

Marble, F. E. & Candel, S. M. 1977 Acoustic disturbance from gas non-uniformities convected through a nozzle. *J. Sound Vib.* **55**, 225–243.

O'Brien, J., Kim, J. & Ihme, M. 2015 Integrated analysis of jet-engine core noise using a hybrid modeling approach. In *23rd AIAA/CEAS Aeroacoustics Conference*, p. 2821.

Papadogiannis, D., Wang, G., Moreau, S., Duchaine, F., Gicquel, L. & Nicoud, F. 2016 Assessment of the indirect combustion noise generated in a transonic high-pressure turbine stage. *J. Eng. Gas Turb. Power* **138**, 1–8.

Pierce, C. D. & Moin, P. 2004 Progress-variable approach for large-eddy simulation of non-premixed turbulent combustion. *J. Fluid Mech.* **504**, 73–97.

Rolland, E. O., De Domenico, F. & Hochgreb, S. 2018 Direct and indirect noise generated by entropic and compositional inhomogeneities. *J. Eng. Gas Turbines Power* **140**, 082604.

Shao, C., Maeda, K. & Ihme, M. 2019 Analysis of core-noise contributions in a realistic gas-turbine combustor operated near lean blow-out. *Proc. Combust. Inst.* Submitted.

Stow, S. R., Dowling, A. P. & Hynes, T. P. 2002 Reflection of circumferential modes in a choked nozzle. *J. Fluid Mech.* **467**, 215–239.

Strahle, W. C. 1978 Combustion noise. *Prog. Energy Combust. Sci.* **4**, 157–176.

Weigand, P., Meier, W., Duan, X., Stricker, W. & Aigner, M. 2005 Investigations of swirl flames in a gas turbine model combustor I. flow field, structures, temperature, and species distributions. *Combust. Flame* **144**, 205–224.